


ARTICLE

<https://doi.org/10.1038/s41467-019-08440-6>

OPEN

Ferromagnetism above 1000 K in a highly cation-ordered double-perovskite insulator Sr_3OsO_6

Yuki K. Wakabayashi¹, Yoshiharu Krockenberger¹, Naoto Tsujimoto², Tommy Boykin¹, Shinji Tsuneyuki², Yoshitaka Taniyasu¹ & Hideki Yamamoto ¹

Magnetic insulators have wide-ranging applications, including microwave devices, permanent magnets and future spintronic devices. However, the record Curie temperature (T_C), which determines the temperature range in which any ferri/ferromagnetic system remains stable, has stood still for over eight decades. Here we report that a highly B-site ordered cubic double-perovskite insulator, Sr_3OsO_6 , has the highest T_C (of ~1060 K) among all insulators and oxides; also, this is the highest magnetic ordering temperature in any compound without 3d transition elements. The cubic B-site ordering is confirmed by atomic-resolution scanning transmission electron microscopy. The electronic structure calculations elucidate a ferromagnetic insulating state with $J_{\text{eff}} = 3/2$ driven by the large spin-orbit coupling of $\text{Os}^{6+} 5d^2$ orbitals. Moreover, the Sr_3OsO_6 films are epitaxially grown on SrTiO_3 substrates, suggesting that they are compatible with device fabrication processes and thus promising for spintronic applications.

¹NTT Basic Research Laboratories, NTT Corporation, 3-1 Morinosato Wakamiya, Atsugi, Kanagawa 243-0198, Japan. ²Department of Physics, The University of Tokyo, 7-3-1 Hongo, Bunkyo-ku, Tokyo 113-0033, Japan. Correspondence and requests for materials should be addressed to Y.K.W. (email: yuuki.wakabayashi.we@hco.ntt.co.jp)

Magnetic insulators have been intensively studied for over 100 years, and they, in particular ferrites, are considered to be the cradle of magnetic exchange interactions in solids. Their wide range of applications include microwave devices¹ and permanent magnets². They are also suitable for spintronic devices owing to their high resistivity³, low magnetic damping⁴, and spin-dependent tunneling probabilities⁵. The Curie temperature (T_C) is the crucial factor determining the temperature range in which any ferri/ferromagnetic system remains stable. However, the record T_C has stood still for over eight decades in insulators and oxides (943 K for spinel ferrite LiFe_5O_8)⁶.

The B-site ordered double-perovskite $\text{A}_2\text{BB}'\text{O}_6$ family includes lots of fascinating magnetic materials such as half-metals^{7–9}, multiferroic materials¹⁰, antiferromagnetic (AFM) materials¹¹, and magnetic insulators^{12–14}. The A site is usually occupied by an alkaline-earth or rare-earth element, and B and B' are transition metal elements. Explorations of magnetism have mainly focused on varying the combination of transition metal elements at B and B' sites, and it has been believed that having them occupied by two different transition metal elements is a prerequisite for a magnetic order at high temperatures⁸. Some 4d or 5d element-containing double-perovskites, e.g., $\text{Sr}_2\text{FeMoO}_6$ ⁷ ($T_C = 415$ K), $\text{Sr}_2\text{CrReO}_6$ ⁹ ($T_C = 634$ K), and $\text{Sr}_2\text{CrOsO}_6$ ¹³ ($T_C = 725$ K), reach a point of ferromagnetic (FM) instability at high temperatures, although the majority of double-perovskites show an AFM order or weak spin-glass behavior¹⁵.

In this work, we show that a highly B-site ordered double-perovskite insulator, Sr_3OsO_6 , surpasses the long-standing T_C record by more than 100 K. In contrast to other 4d or 5d double-perovskites that follow the above-mentioned criteria, we discovered FM ordering above 1000 K in Sr_3OsO_6 , in which only one 5d transition metal element occupies the B sites. Remarkably, the T_C of Sr_3OsO_6 (~1060 K) is about ten times higher than the previous highest magnetic transition temperature in double-perovskites including only one transition element ($\text{Sr}_2\text{MgOsO}_6$, AFM, $T_N = 110$ K)¹⁶. We revealed this B-site ordering using atomic-resolution scanning transmission electron microscopy. The density functional

theory (DFT) calculations suggest that the large spin–orbit coupling (SOC) of $\text{Os}^{6+} 5d^2$ orbitals drives the system toward a $J_{\text{eff}} = 3/2$ FM insulating state^{17–19}. Moreover, the Sr_3OsO_6 is the epitaxially grown osmate, which connotes that it is compatible with device fabrication processes and thus promising for spintronic applications.

Results

Epitaxial growth and crystallographic analyses. High-quality single-crystalline B-site-ordered double-perovskite Sr_3OsO_6 films (300-nm thick) were epitaxially grown on (001) SrTiO_3 substrates with an abrupt substrate/film interface in a custom-designed molecular beam epitaxy (MBE) setup capable of precisely controlling elemental fluxes even for elements with high melting points, e.g., Os (3033 °C) (Methods). Maintaining a precise flux rate for each constituent cation (Os and Sr) with a simultaneous supply of O_3 is essential for avoiding deterioration of the magnetic properties as a deviation of only 2% from the optimal Os/Sr ratio is fatal (Methods).

High-resolution scanning transmission electron microscopy (STEM) and transmission electron diffraction (TED), combined with high-resolution reciprocal space mapping (HRRSM) and reflection high-energy electron diffraction (RHEED), ascertained a cubic double-perovskite structure^{8,12,20} (Methods). As schematically shown in Fig. 1a, d (viewed along [100] and [110] directions), Sr- or Os-occupied, fully Sr-occupied, fully Os-occupied, and fully oxygen-occupied columns exist. The STEM images overtly demonstrate that these columns are arranged in a spatially ordered sequence. Since the intensity in the high-angle annular dark-field (HAADF)-STEM image is proportional to $\sim Z^n$ ($n \sim 1.7\text{--}2.0$, and Z is the atomic number), in Fig. 1b, the white spheres and gray ones are assigned to Sr- ($Z = 38$) or Os- ($Z = 76$) occupied and fully Sr-occupied columns, respectively. In Fig. 1e, the white spheres and gray ones are assigned to fully Os-occupied and fully Sr-occupied columns, respectively. In contrast to HAADF-STEM, Oxygen is emphasized in annular bright-field (ABF)-STEM images. Accordingly, Oxygen ions occupying the

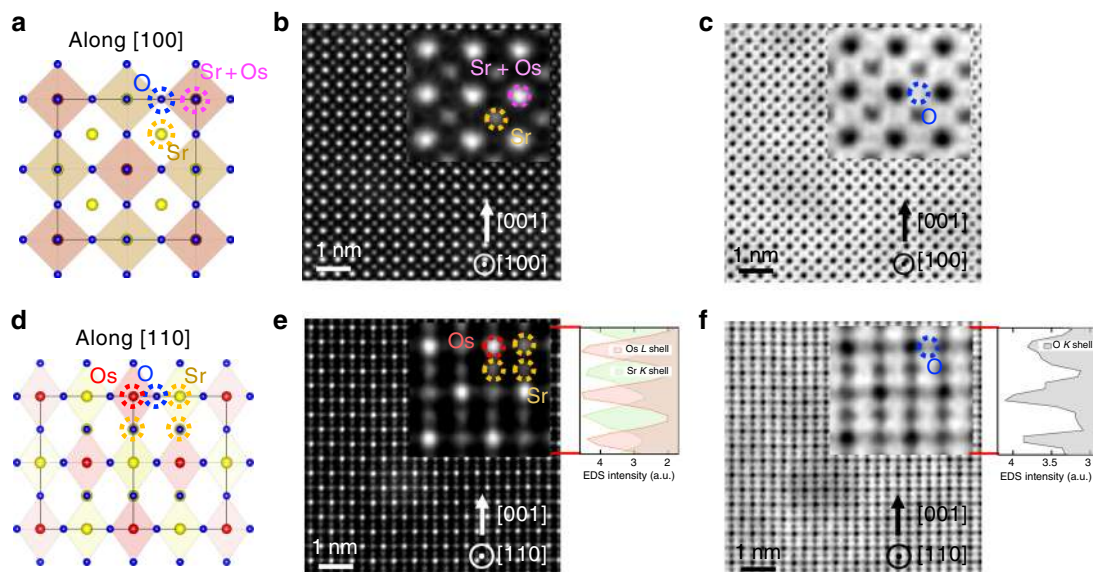


Fig. 1 Atomic-resolution STEM images of a Sr_3OsO_6 film. **a** Schematic diagram of the Sr_3OsO_6 viewed along the [100] direction. **b, c** HAADF-STEM (**b**) and ABF-STEM (**c**) images near the center of the Sr_3OsO_6 layer along the [100] direction. **d** Schematic diagram of the Sr_3OsO_6 viewed along the [110] direction. **e, f** HAADF-STEM (**e**) and ABF-STEM (**f**) images near the center of the Sr_3OsO_6 layer along the [110] direction. The scale bars are 1 nm. The insets in **b, c, e**, and **f** show enlarged views together with EDS-STEM intensity profiles along the [001] direction. In all figures, purple, yellow, red, and blue dotted circles indicate Sr- or Os-occupied, fully Sr-occupied, fully Os-occupied, and fully oxygen-occupied columns, respectively

expected positions are clearly visible (labeled O (insets of Fig. 1c, f)). The energy dispersive X-ray spectroscopy (EDS)-STEM intensity profiles along the [001] direction shown in Fig. 1e and f complementarily confirm the above elemental assignments. The peak positions in the EDS profile of the Os *L* shell, Sr *K* shell, and oxygen *K* shell agree well with the Os, Sr, and oxygen positions, respectively, determined by STEM. The STEM observation revealed the rock-salt type order of Os⁶⁺, whereas the hexavalent state of Os is confirmed by X-ray photoemission spectroscopy (XPS) measurements (METHODS), to an excellent extent, and this ordering is driven by the large difference in the electronic charges and ionic radii between Sr²⁺ and Os⁶⁺²¹. Consequently, the experimentally derived crystal structure does not allow for Os–O–Os paths. Therefore, advanced mechanisms need to be considered, since the Goodenough–Kanamori rules²², which well predict magnetic interactions between two next-nearest-neighbor magnetic cations through a nonmagnetic anion, do not cover the theoretical framework for the FM order in Sr₃OsO₆.

Magnetic properties. Figure 2a, b shows the temperature dependence of magnetization versus the magnetic field (*M–H*) of a Sr₃OsO₆ film. The hysteretic response of the Sr₃OsO₆ film shows a soft magnetic behavior with the small coercive field of ~100 Oe at 1.9 K (Fig. 2b), and the saturation magnetization at 70,000 Oe (Fig. 2a) decreases with increasing temperature. The saturation magnetization persists up to 1000 K [limit of measurement range (Methods)], indicating *T*_C > 1000 K. Figure 2c shows the magnetization versus temperature (*M–T*) curve with *H* = 2000 Oe. In Fig. 2c, we also plot the spontaneous magnetization as a function of temperature. The *T*_C value, estimated from the extrapolation of the *M–T* curve to the zero magnetization axis, is about 1060 K (Fig. 2c). This is the highest *T*_C among all insulators and oxides, and the highest magnetic ordering temperature in any compound without 3*d* transition elements²³.

Noteworthy, the saturation magnetization of Sr₃OsO₆ (~49 emu/cc at 1.9 K) is significantly smaller than that for typical magnetic metals; e.g., Nd₂Fe₁₄B (~1280 emu/cc), SmCo₅ (~860 emu/cc) and Alnico 5 (~1120 emu/cc)²⁴, and typical ferrites; e.g., CoFe₂O₄ (~430 emu/cc), Y₃Fe₅O₁₂ (~170 emu/cc) and LiFe₅O₈ (~390 emu/cc)⁶. The small saturation magnetization, unique to Sr₃OsO₆, may encourage the development of spintronic devices utilizing small stray fields and low-energy spin-transfer-torque switching²⁵, which are advantageous for high-density integration and low-power consumption. This small saturation magnetization is, most likely, associated with the low composition ratio of Os in Sr₃OsO₆. The saturation magnetic moment of Os at 1.9 K was estimated to be 0.77 μ_B/Os, which is smaller than the

expected value of the spin-only magnetic moment of 2 μ_B for the Os⁶⁺ (5*d*² *t*_{2g}²) state with *S* = 1. This apparent deviation requires that SOC has to be taken into account, which is often the case with 5*d* systems^{18,26,27}.

Electrical properties. While such high *T*_C is common for systems with free charge carriers, e.g., Fe₃O₄ and Co, their absence in Sr₃OsO₆ requires other exchange mechanisms. The temperature dependence of resistivity (*ρ*) for a Sr₃OsO₆ film is shown in Fig. 3a. It increases with decreasing temperature and it exceeds the measurable range below 120 K. The electronic charge carriers [5*d* electrons in the Os⁶⁺ state] move by hopping between localized electronic states, and this is supported by ln(*ρ*) ∝ *T*^{-1/4} [variable range hopping (VRH) model] (Fig. 3b) along with the high resistivity value [*ρ*(300 K) = 75 Ω cm]. Other mechanisms, e.g., ln(*ρ*) ∝ *T*^{-1/2} [Efros–Shklovskii Hopping (ESH) model] and ln(*ρ*) ∝ *T*⁻¹ [thermal activation (TA) model], are not supported by the electronic transport measurements. Figure 3c shows electron energy loss spectroscopy (EELS) spectra of a Sr₃OsO₆ film measured at three different positions as indicated in the cross-sectional STEM image (inset of Fig. 3c) with a spot size of ~4 nm. The EELS spectrum of a material corresponds to the loss function *Im*(-1/*ε*), where *ε* is a complex dielectric function. The three EELS spectra (Fig. 3c) taken of Sr₃OsO₆ are almost identical, indicating that electronic states are uniform in the entire Sr₃OsO₆ film. The optical bandgap (indicated by the black arrow), at which EELS intensities start to increase^{28,29}, is ~2.65 eV. Accordingly, models based on the double exchange interaction where itinerant electrons are driving the magnetic order, can be ruled out as the origin of ferromagnetic order in Sr₃OsO₆. In addition, the long distance between nearest Os atoms (5.81 Å) renders the possibility of direct exchange interactions unlikely^{30,31}.

Electronic-structure calculations. We analyzed the electronic and magnetic states of Sr₃OsO₆ by DFT with SOC (METHODS) using calculations with the Perdew–Burke–Ernzerhof (PBE) functional³². Canted FM order (Fig. 4a) was found to have the lowest total energy among many possible magnetic arrangements. However, the energy differences between the canted FM order and the collinear FM (Supplementary Fig. 10a), (001) AFM (Supplementary Fig. 10b), and (111) AFM orders (Supplementary Fig. 10c) are very small (~3.6 meV per atom, ~1.4 meV per atom and ~0.29 meV per atom, respectively), implying a competition among these orders. Note that canted magnetic orders have been reported in other Os containing double-perovskites^{11,33}. The optical bandgap determined by GGA-PBE + *U* + SOC calculations of Sr₃OsO₆ with the canted FM order is ~0.69 eV, and this

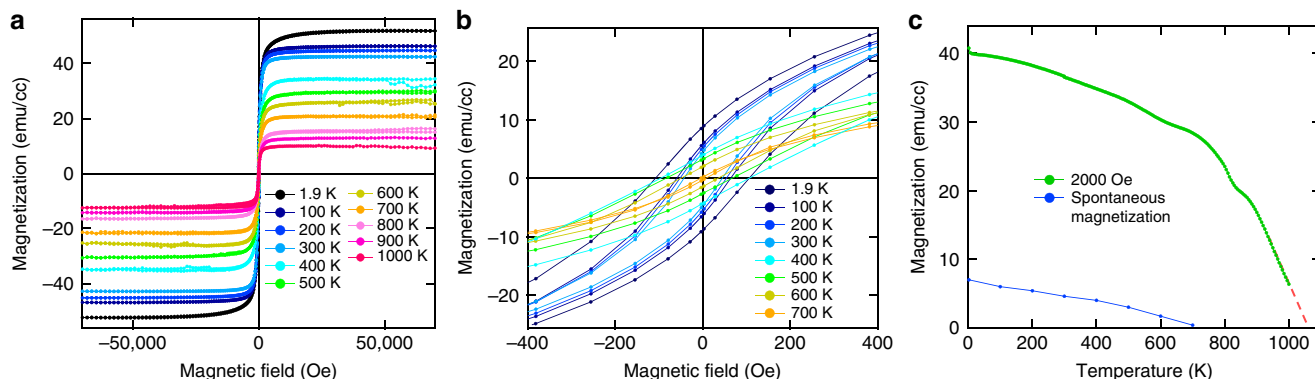


Fig. 2 Magnetic properties of a Sr₃OsO₆ film. **a** In-plane *M–H* curves at 1.9 up to 1000 K for a Sr₃OsO₆ film grown on (001) SrTiO₃. Here, *H* was applied to the [100] direction. **b** Close-up near the zero magnetic field in **a**. **c** *M–T* curve with *H* = 2000 Oe applied to the [100] direction for a Sr₃OsO₆ film grown on (001) SrTiO₃. Spontaneous magnetization deduced from Fig. 2b as a function of temperature is also shown

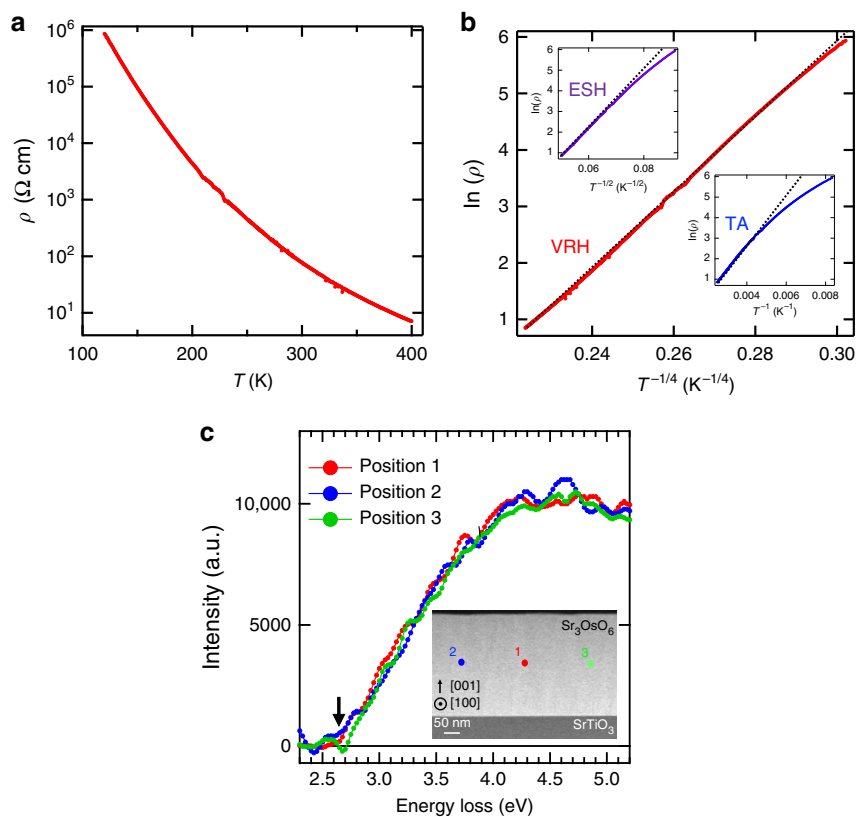


Fig. 3 Resistivity and dielectric properties of a Sr_3OsO_6 film. **a** ρ - T curve for a Sr_3OsO_6 film. **b** Logarithm of ρ versus $T^{-1/4}$ plot, corresponding to the VRH model. The insets of **b** show the logarithm of ρ versus $T^{-1/2}$ and T^{-1} plots, corresponding to the ESH and TA models, respectively. The black dashed lines in **b** are guides to the eye. **c** The EELS spectra of a Sr_3OsO_6 film measured at the spots indicated in the cross-sectional STEM image (inset). The background was corrected with a power-law fit from 2 to 2.3 eV

corresponds to an insulating state (Fig. 4b, c). With $U + \text{SOC}$, the $t_{2g\uparrow}$ states are split into effective total angular momenta $J_{\text{eff}} = 3/2$ (doublet) and $J_{\text{eff}} = 1/2$ (singlet) states while opening a gap. The $J_{\text{eff}} = 3/2$ states are fully occupied with two $5d$ electrons per Os^{6+} , resulting in the insulating state. Note that these calculations reveal a metallic ground state (i.e., no gap at the Fermi energy (E_F)), if $U = 0$ eV. This is because the band dispersions of $J_{\text{eff}} = 3/2$ and $J_{\text{eff}} = 1/2$ states are greater than the spin-orbit splitting. The calculated magnetic moment of osmium is $1.56 \mu_B/\text{Os}$, which is closer to the experimentally determined value ($0.77 \mu_B/\text{Os}$) as compared with the spin-only magnetic moment ($2 \mu_B/\text{Os}$). We also calculated the element-specific partial density-of-state (PDOS) of Sr_3OsO_6 for the canted FM order by the Heyd-Scuseria-Ernzerhof (HSE) functional + SOC method (Supplementary Fig. 11) to properly implement the interaction length scale found in solids. Consequently, the DFT calculations with the HSE functional have superior prediction capabilities regarding band gaps of insulators³⁴. The bandgap estimated by the HSE + SOC method (~ 1.41 eV) is closer to the experimentally obtained one (~ 2.65 eV) than that estimated by the GGA-PBE + $U + \text{SOC}$ calculations (~ 0.69 eV). Although further work is required to reveal the underlying mechanisms driving the FM order in Sr_3OsO_6 , our calculations provide information on the magnetic arrangement at the ground state and how the energy gap is opened by the interplay between Coulomb repulsion (U) and SOC.

Discussion

The origin of the robust ferromagnetism in this magnetic insulator (Sr_3OsO_6) remains murky, and it appears to be a challenge

to reveal the underlying electronic exchange mechanisms. The extended superexchange paths (Os-O-Sr-O-Os), which are well recognized to drive the magnetic order in Os containing double-perovskites^{30,31,35}, are one possible origin of the ferromagnetism. Since a high magnetic ordering temperature through the extended superexchange paths requires a strong p - d hybridization³⁵, further investigations into the electronic structures of Sr_3OsO_6 , such as X-ray magnetic circular dichroism (XMCD), are required. Nevertheless, our DFT calculations with both the PBE (Fig. 4c) and HSE (Supplementary Fig. 11) functionals imply a non-negligible p - d hybridization.

Attention should be paid to the excellent Os order, since cationic disorder deteriorates magnetic ordering in magnetic insulators³⁶⁻³⁸. Besides, Ca_3OsO_6 shows an antiferromagnetic order below 50 K²¹, despite its high Os order and being isoelectronic to Sr_3OsO_6 . A remarkable difference between Sr_3OsO_6 and Ca_3OsO_6 is their crystal structure (Ca_3OsO_6 is monoclinic with tilted OsO_6 octahedrons). Such a difference in magnetic order despite the isoelectronic structures was also reported for the isoelectronic pair SrRuO_3 (pseudo-cubic perovskite, ferromagnetic metal) and CaRuO_3 (orthorhombic perovskite, paramagnetic metal)³⁹, and the difference in the magnetic order in SrRuO_3 and CaRuO_3 is thought to be associated with the strength of the perovskite distortion. The network morphology hosting the mechanisms of exchange interactions is subject to such distortions, thus, likely driving Ca_3OsO_6 towards an antiferromagnetic instability. In addition, the cubic double-perovskite structure, in which only one $5d$ transition metal element occupies the B site, possesses 12 nearest neighbor magnetic ions in contrast to other $4d$ or $5d$ element-containing double-perovskites, in which both B and B' sites are occupied by two different transition metal

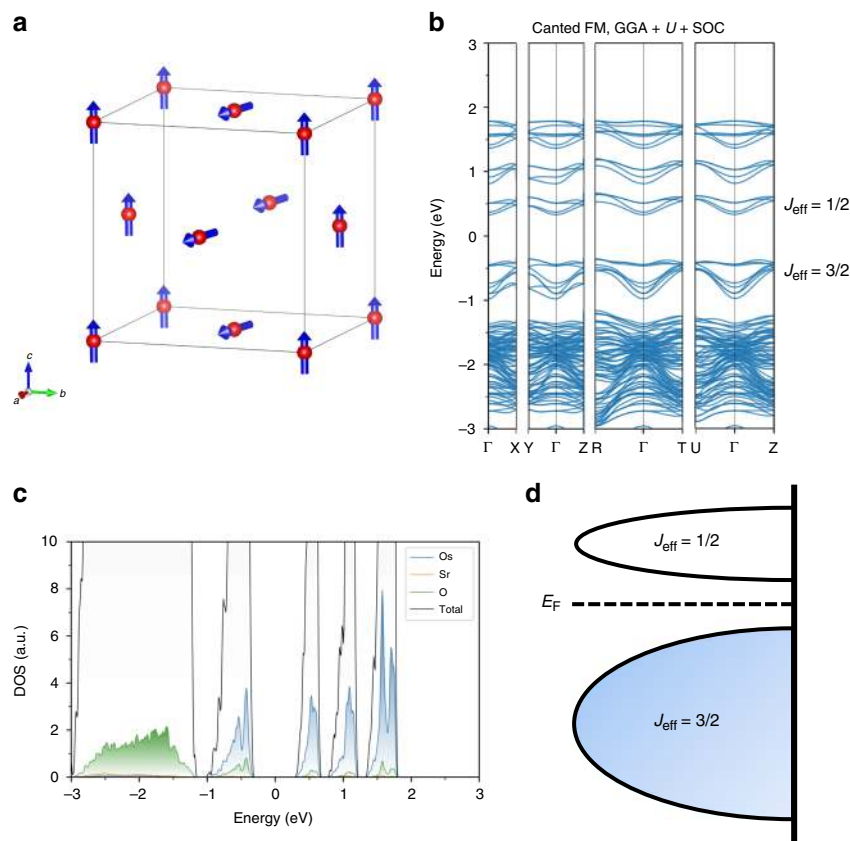


Fig. 4 Electronic-structure calculations with the PBE functional. **a** Schematic diagram of the magnetic ground state (canted FM order) of Sr_3OsO_6 obtained from the DFT calculation. In **a**, red spheres and blue arrows indicate Os atoms and magnetic moments of Os atoms, respectively, and the Sr and O atoms are omitted for simplicity. **b** The band structures for Sr_3OsO_6 with the canted FM order calculated by GGA + U + SOC. **c** The element-specific partial density-of-state (PDOS) for the canted FM order calculated by GGA + U + SOC. In **c**, blue, orange, and green curves indicate the density-of-states per one Os, Sr, and O atoms, respectively. In **b** and **c**, the origin of energy was taken at the center of the bandgap. **d** Schematic energy diagrams for the Os $5d^2$ configurations. In **d**, only PDOS for Os is taken into account and the contributions by Sr and O are omitted for simplicity

elements, e.g., $\text{Sr}_2\text{FeMoO}_6$ ($T_C = 415\text{ K}$)⁷, $\text{Sr}_2\text{CrReO}_6$ ($T_C = 634\text{ K}$)⁹ and $\text{Sr}_2\text{CrOsO}_6$ ($T_C = 725\text{ K}$)¹³. This could be one of the reasons for the robust ferromagnetism in Sr_3OsO_6 as predicted for halide double-perovskites⁴⁰. Therefore, we suggest that the high Os order with the cubic structure plays an essential role in the robust ferromagnetism achieved in Sr_3OsO_6 .

Our current findings in epitaxial Sr_3OsO_6 films—an extraordinarily high T_C of 1060 K, $J_{\text{eff}} = 3/2$ insulating state, rock-salt type Os^{6+} order and small magnetic moment—enrich the family of ferri/ferromagnetic insulators. Although the underlying electronic exchange mechanisms driving the robust FM order in Sr_3OsO_6 remain murky, applications of Sr_3OsO_6 to oxide-electronics^{41,42} beyond the current ferrite technology are feasible.

Methods

Growth of Sr_3OsO_6 on SrTiO_3 . We grew the high-quality epitaxial B-site ordered double-perovskite (001) Sr_3OsO_6 films (300- or 250-nm thick) on (001) SrTiO_3 substrates (CrysTec GmbH) in a custom-designed molecular beam epitaxy (MBE) system^{43,44} (Supplementary Fig. 1a). After cleaning with CHCl_3 (10 min, two times) and acetone (5 min) by an ultrasonic cleaner, the SrTiO_3 substrate was introduced in the MBE growth chamber. After degassing the substrate at 400 °C for 30 min and successive thermal cleaning at 650 °C for 30 min, we grew a Sr_3OsO_6 film. The growth temperature was 650 °C. The oxidation during the growth was carried out with O_3 gas (non-distilled, ~10% concentration) from a commercial ozone generator as a flow rate of 2 sccm. After the growth, films were cooled to room temperature under ultra-high vacuum (UHV). The MBE system is equipped with multiple e-beam evaporators (Hydra, Thermionics) for Sr and Os. Note that to avoid a formation of OsO_4 , which is highly toxic, we used Os chunks with a radius of about 3 mm (not Os powder), which are stable in air at room temperature. The electron impact emission spectroscopy (EIES) sensor (Guardian, Inficon) is located next to the sample heater in the MBE in the same horizontal plane. The

sensor head is equipped with a filament, which generates thermal electrons for the excitation of Sr and Os atoms. Optical band-pass filters are used for element-specific detection of the excited optical signals, since the emitted light spectra are characteristic for Sr and Os. The EIES sensor is equipped with photomultipliers (PMTs) located outside of the vacuum chamber that convert optical signals into electrical signals. The Sr and Os fluxes measured by EIES were kept constant (Supplementary Fig. 1b) by the proportional-integral-derivative (PID) control of the evaporation source power supply. We optimized the flux ratio of Sr and Os to ascertain Sr_3OsO_6 films with a high saturation magnetic moment. Supplementary Fig. 2 shows the in-plane M - H curves at 300 K for Sr_3OsO_6 films grown with different flux ratios of Sr and Os. The saturation magnetic moment of the film grown with the flux ratio of Sr:Os = 2.05:1 is ten or more times larger than those for the films grown with the flux ratio of Sr:Os = 2.05:1.02 and 2.05:0.98. This means that the magnetic properties of Sr_3OsO_6 films are very sensitive to the Sr/Os ratio and that well-controlled Sr and Os fluxes during the growth are important for the high saturation magnetic moment. Therefore, in this study, we set the flux ratio of Sr:Os at 2.05:1.

The cubic crystal structure of Sr_3OsO_6 is illustrated in Supplementary Fig. 3a. Supplementary Fig. 3b,c show reflection high-energy electron diffraction (RHEED) patterns of a Sr_3OsO_6 thin film surface, where the sharp streaky patterns with clear surface reconstruction indicate the growth of the Sr_3OsO_6 film in a layer-by-layer manner, leading to the high crystalline quality of the film. Notably, [011] diffractions are not seen (Supplementary Fig. 3b) due to extinction rules, indicating the formation of a cubic B-site ordered double-perovskite^{8,12,20}. The cubic structure model is further supported by high-resolution X-ray reciprocal space mapping (HRRSM) (Supplementary Fig. 3d): the in-plane and out-of-plane lattice constants of Sr_3OsO_6 are identical within the resolution limits (8.24 ± 0.03 and $8.22 \pm 0.03\text{ \AA}$, respectively). It is therefore reasonable that the Sr_3OsO_6 films are epitaxially but not coherently grown on the SrTiO_3 (3.905 Å) substrate.

Transmission electron microscopy and transmission electron diffraction.

High-angle annular dark-field (HAADF), annular bright-field (ABF) scanning transmission electron microscopy (STEM) images, and transmission electron diffraction (TED) patterns were taken with a JEOL JEM-ARM 200F microscope.

Electron energy loss spectroscopy (EELS) spectra of a Sr_3OsO_6 film were recorded from three spots with a ~ 4 -nm diameter also with a JEOL JEM-ARM 200F microscope.

Supplementary Figs. 3e–g show cross-sectional HAADF-STEM images of a Sr_3OsO_6 film taken along the [100] direction. At a glance, one can recognize that a single-crystalline Sr_3OsO_6 film with an abrupt substrate/film interface has been grown epitaxially on a (001) SrTiO_3 substrate, as expected from the RHEED. Misfit dislocations at the $\text{Sr}_3\text{OsO}_6/\text{SrTiO}_3$ interface (Supplementary Fig. 3g) are due to the $\sim 5\%$ larger lattice constant of the perovskite Sr_3OsO_6 lattice ($8.23 \text{ \AA}/2 = 4.115 \text{ \AA}$) than that of SrTiO_3 (3.905 \AA). The cubic crystal structure of Sr_3OsO_6 was also confirmed by the STEM analysis. In addition to the [100] direction (Supplementary Figs. 3e–g), the epitaxial growth of the Sr_3OsO_6 layer on the SrTiO_3 substrate was also confirmed by STEM images taken along the [110] direction (Supplementary Figs. 4a–c). The rock-salt type order of Os^{6+} (Fig. 1) is observed to an excellent extent (Supplementary Figs. 4d,e).

Supplementary Fig. 5 shows the TED pattern for a Sr_3OsO_6 film taken along the [110] direction. The diffraction pattern agrees very well with the calculated diffraction pattern for the ideal cubic B-site ordered double-perovskite structure shown in Supplementary Fig. 3a. The extinction rules for a fully B-site ordered double-perovskite demand that either even (hkl) or odd (hkl) peaks are permitted²⁰—and that is exactly what is seen here, confirming the cubic B-site ordered double-perovskite structure.

Chemical composition of a Sr_3OsO_6 film. Supplementary Fig. 6a shows the depth profile of the chemical composition of a Sr_3OsO_6 film (250-nm thick) estimated from Rutherford backscattering spectroscopy (RBS). The chemical composition of the Sr_3OsO_6 layer is uniform ($\text{Sr}:\text{Os}:\text{O} = 2.7 \pm 0.1:1.15 \pm 0.05:6.15 \pm 0.4$). The concentrations of Os and Oxygen are slightly larger than those for an ideal composition ($\text{Sr}:\text{Os}:\text{O} = 3:1:6$). This difference may originate from the non-stoichiometry and existence of a small amount of paramagnetic metallic OsO_2 ^{45–47}, which was observed in the X-ray diffraction (XRD) measurements, as described below. To exclude the possibility of the contamination by magnetic impurities, we performed EDS measurement for a Sr_3OsO_6 film (Supplementary Fig. 6b). There are no other peaks except for Sr, Os, Ti, O, and C, which confirms the absence of magnetic impurities.

X-ray diffraction. We performed θ – 2θ and reciprocal space map XRD measurements of the Sr_3OsO_6 films with a Bruker D8 diffractometer using monochromatic $\text{Cu K}\alpha_1$ radiation at room temperature. In Supplementary Fig. 6c, we show the θ – 2θ XRD pattern for a Sr_3OsO_6 film on (001) SrTiO_3 . In addition to the diffraction peaks of the SrTiO_3 substrates, (002) and (004) diffractions from Sr_3OsO_6 are clearly observed. No (001) and (003) diffractions from Sr_3OsO_6 are seen due to the extinction rules. Note that traces of OsO_2 , which is known as a paramagnetic metal^{45–47}, are detected as indicated by *. The XRD intensities of OsO_2 are about 700 times smaller than those of Sr_3OsO_6 , and segregation of OsO_2 is not discernible in the STEM images, indicating that the volume fraction of OsO_2 (paramagnetic metal^{45–47}) is negligible. Therefore, Sr_3OsO_6 dominates the magnetic response of the film.

X-ray photoemission measurements. X-ray photoemission spectroscopy (XPS) is one of the most powerful methods to determine the valence of Os in compounds^{48,49}, since the $4f_{7/2}$ core level binding energies in Os compounds with well-defined oxidation states are known. An ULVAC-PHI Model XPS5700 with a monochromatized $\text{Al K}\alpha$ (1486.6 eV) source operated at 200 W was used for the experiments. The scale of binding energy was calibrated against the C 1s line (284.6 eV). Supplementary Fig. 7 shows the Os 4f spectrum of a Sr_3OsO_6 film at 300 K. The observed $4f_{7/2}$ binding energy (54.1 eV) is close to the reported values for those of Os^{6+} states (53.2–53.8 eV) and far from those for Os^{2+} states (49.7 eV), Os^{3+} states (50.4–51.0 eV), Os^{4+} states (51.7–52.3 eV), and Os^{8+} states (55.9–56.3 eV)^{48,49}. Accordingly, the hexavalent state of Os (Os^{6+}) is supported. Note that a shoulder structure at ~ 53 eV may originate from a surface layer formed due to the slightly hygroscopic nature of Sr_3OsO_6 because the sample was transferred to the XPS apparatus in atmosphere.

Resistivity measurements. Resistivity was measured using the four-probe method in a Physical Property Measurement System (PPMS) Dynacool sample chamber. The Ag electrodes were deposited on a Sr_3OsO_6 surface and connected to an Agilent 3458A Multimeter.

Magnetic measurements. The magnetization measurements for Sr_3OsO_6 films were performed with a Quantum Design MPMS3 SQUID-VSM magnetometer. Using a quartz sample holder (oven sample holder), we measured the M – T curves while increasing the temperature from 1.9 (300) to 300 (1000) K with $H = 2000$ Oe applied along the [100] or [110] direction. In the M – T measurements, M was measured with increasing temperature after the sample was cooled to 1.9 (300) K from 300 (1000) K without a magnetic field. We also measured M – H curves at 1.9–300 K (400–1000 K) using the quartz sample holder (oven sample holder).

To check the accuracy of the measurement temperature in the MPMS SQUID-VSM magnetometer, we measured the magnetic properties of a pure Ni reference

plate (Quantum Design Part Number: 4505–155). The M – H curves at 300 and 1000 K show FM and paramagnetic response, respectively (Supplementary Fig. 8a), and the magnetization of Ni rapidly increases between 623 and 629 K (Supplementary Fig. 8b). These results indicate that the T_C of Ni is between 623 and 629 K. This is consistent with the T_C value in the literature (627 K)⁵⁰. Thus, the error in the measurement temperature in the MPMS SQUID-VSM magnetometer is less than ± 4 K.

Supplementary Fig. 8c shows the in-plane M – H curves at 1.9, 300, and 1000 K of a SrTiO_3 substrate. They show only a linear diamagnetic response at 300 and 1000 K. The nonlinear magnetic response near the zero magnetic field at 1.9 K indicates the existence of paramagnetic impurities in the SrTiO_3 substrates. In Fig. 2, the linear diamagnetic response of the magnetic moment for the SrTiO_3 substrate was subtracted from the raw $M(H)$ and $M(T)$.

Supplementary Fig. 8d shows the M – T curve with $H = 2000$ Oe for the oven sample holder without a sample. The curve shows a dip structure at around 800 K. This means that the dip structure in the M – T curve at around 800 K for the Sr_3OsO_6 film (Fig. 2c) is an unavoidable experimental artifact.

The magnetic properties of Sr_3OsO_6 at 300 K did not change much after it was heated to 1000 K as shown in Supplementary Fig. 9a. This means that heating to 1000 K does not affect much its magnetic properties.

Although the Sr_3OsO_6 films were epitaxially grown on the SrTiO_3 substrates, the shapes of the in-plane M – H curves measured with H applied to the [100] or [110] direction are identical (Supplementary Fig. 9b). This indicates that the in-plane magnetic anisotropy of the Sr_3OsO_6 film is negligibly small. This small magnetic anisotropy might be related to the misfit dislocations (Supplementary Fig. 3e–g), which often decrease the magnetic anisotropy of magnetic insulators^{36–38}.

The electronic-structure calculations. The electronic-structure calculations were based on density functional theory (DFT). The calculations were performed by using the Vienna Ab initio Simulation Package (VASP)^{51,52} with the projector augmented-wave (PAW)^{53,54} method and the Perdew–Burke–Ernzerhof (PBE) functional³² within the generalized gradient approximation (GGA)⁵⁵. To describe the localization of Os $5d$ electrons accurately, we used the DFT + U calculations⁵⁶. The value of the screened Coulomb interaction $U = 3$ eV was used for the Os atoms. This value is comparable to reported values for Os containing double-perovskites (2–4 eV)^{14,18,19,31}. The contribution of the spin–orbit coupling (SOC) was also included in our calculations. The crystal structure was optimized for the conventional unit cell (40 atoms) of Sr_3OsO_6 whose lattice constant was fixed to the experimental value 8.23 Å. We performed the optimization until all forces on the atoms become smaller than 10^{-5} eV/Å with a Γ -centered $2 \times 2 \times 2$ k -point grid and cut-off energy of 800 eV. The total energies and electronic structures were calculated with the optimized crystal structures resulting in the canted FM ground state (Fig. 4a).

By comparing the total energy of the magnetic ground state (canted FM order) (Fig. 4a) with those of the collinear FM order (Supplementary Fig. 10a), the (001) AFM order (Supplementary Fig. 10b) and the (111) AFM order (Supplementary Fig. 10c), we found that the energy differences between the canted FM order and the other orders are very small (~ 3.6 , ~ 1.4 , and ~ 0.29 meV per atom, respectively), implying a competition among these orders.

We also calculated the element-specific partial density-of-state (PDOS) of Sr_3OsO_6 for the canted FM order by the Heyd–Scuseria–Ernzerhof (HSE) + SOC method (Supplementary Fig. 11).

Data availability

The data that support the plots in this paper and other findings of this study are available from the corresponding author upon request.

Received: 7 August 2018 Revised: 20 December 2018 Accepted: 8 January 2019

Published online: 12 February 2019

References

- Naito, Y. & Suetake, K. Application of ferrite to electromagnetic wave absorber and its characteristics. *IEEE Trans. Microw. Theory Tech.* **19**, 65 (1973).
- Tenaud, P., Morel, A., Kools, F., Le Breton, J. M. & Lechevallier, L. Recent improvement of hard ferrite permanent magnets based on La-Co substitution. *J. Alloy. Comp.* **370**, 331 (2004).
- Avci, C. O. et al. Current-induced switching in a magnetic insulator. *Nat. Mater.* **16**, 309 (2017).
- Kagiwara, Y. et al. Transmission of electrical signals by spin-wave interconversion in a magnetic insulator. *Nature* **464**, 262 (2010).
- Moodera, J. S., Hao, X., Gibson, G. A. & Meservey, R. Electron-spin polarization in tunnel junctions in zero applied field with ferromagnetic EuS barriers. *Phys. Rev. Lett.* **61**, 637 (1988).

6. Posnjak, E. & Barth, T. F. W. A new type of crystal fine-structure: lithium ferrite ($\text{Li}_2\text{O}\cdot\text{Fe}_2\text{O}_3$). *Phys. Rev.* **38**, 2234 (1931).
7. Kobayashi, K.-I., Kimura, T., Sawada, H., Terakura, K. & Tokura, Y. Room-temperature magnetoresistance in an oxide material with an ordered double-perovskite structure. *Nature* **395**, 677 (1998).
8. Chen, W.-t et al. A half-metallic A- and B-site-ordered quadruple perovskite oxide $\text{CaCu}_3\text{Fe}_2\text{Re}_2\text{O}_{12}$ with large magnetization and a high transition temperature. *Nat. Commun.* **5**, 3909 (2014).
9. Kato, H. et al. Metallic ordered double-perovskite $\text{Sr}_2\text{CrReO}_6$ with maximum Curie temperature of 635 K. *Appl. Phys. Lett.* **81**, 328 (2002).
10. Sakai, M. et al. Multiferroic thin film of $\text{Bi}_2\text{NiMnO}_6$ with ordered double-perovskite structure. *Appl. Phys. Lett.* **90**, 072903 (2007).
11. Yan, B. et al. Lattice-site-specific spin dynamics in double perovskite $\text{Sr}_2\text{CoOsO}_6$. *Phys. Rev. Lett.* **112**, 147202 (2014).
12. Iwasawa, H. et al. Strong correlation effects of the Re 5d electrons on the metal-insulator transition in $\text{Ca}_2\text{FeReO}_6$. *Phys. Rev. B* **71**, 075106 (2005).
13. Krockenberger, Y. et al. $\text{Sr}_2\text{CrOsO}_6$: End point of a spin-polarized metal-insulator transition by 5d band filling. *Phys. Rev. B* **75**, 020404(R) (2007).
14. Feng, H. L. et al. $\text{Ba}_2\text{NiOsO}_6$: a Dirac-Mott insulator with ferromagnetism near 100 K. *Phys. Rev. B* **94**, 235158 (2016).
15. Battle, P. D., Gibb, T. C., Herod, A. J., Kim, S.-H. & Munns, P. H. Investigation of magnetic frustration in A_2FeMO_6 (A = Ca, Sr, Ba; M = Nb, Ta, Sb) by magnetometry and mossbauer spectroscopy. *J. Mater. Chem.* **5**, 865 (1995).
16. Yuan, Y. et al. High-pressure synthesis, crystal structures, and magnetic properties of 5d double-perovskite oxides $\text{Ca}_2\text{MgOsO}_6$ and $\text{Sr}_2\text{MgOsO}_6$. *Inorg. Chem.* **54**, 3422 (2015).
17. Erickson, A. S. et al. Ferromagnetism in the Mott insulator $\text{Ba}_2\text{NaOsO}_6$. *Phys. Rev. Lett.* **99**, 016404 (2007).
18. Xiang, H. J. & Whangbo, M.-H. Cooperative effect of electron correlation and spin-orbit coupling on the electronic and magnetic properties of $\text{Ba}_2\text{NaOsO}_6$. *Phys. Rev. B* **75**, 052407 (2007).
19. Gangopadhyay, S. & Pickett, W. E. Spin-orbit coupling, strong correlation, and insulator-metal transitions: The $J_{\text{eff}} = 3/2$ ferromagnetic Dirac-Mott insulator $\text{Ba}_2\text{NaOsO}_6$. *Phys. Rev. B* **91**, 045133 (2015).
20. Manako, T. et al. Epitaxial thin films of ordered double perovskite $\text{Sr}_2\text{FeMoO}_6$. *Appl. Phys. Lett.* **74**, 2215 (1999).
21. Feng, H. L. et al. High-pressure crystal growth and electromagnetic properties of 5d double-perovskite Ca_3OsO_6 . *J. Solid State Chem.* **201**, 186 (2013).
22. Goodenough, J. B. *Magnetism and the Chemical Bond* (Wiley, New York, 1963).
23. Rodriguez, E. E. et al. High temperature magnetic ordering in the 4d perovskite SrTcO_3 . *Phys. Rev. Lett.* **106**, 067201 (2011).
24. Coey, J. M. D. Hard magnetic materials: a perspective. *IEEE Trans. Magn.* **47**, 4671 (2011).
25. Stiles, M. D. & Zangwill, A. Anatomy of spin-transfer torque. *Phys. Rev. B* **66**, 014407 (2002).
26. Calder, S. et al. Spin-orbit-driven magnetic structure and excitation in the 5d pyrochlore $\text{Cd}_2\text{Os}_2\text{O}_7$. *Nat. Commun.* **7**, 11651 (2016).
27. Kim, B. J. et al. Phase-sensitive observation of a spin-orbital Mott state in Sr_2IrO_4 . *Science* **323**, 1329 (2009).
28. Oleshko, V., Amkreutz, M. & Overhof, H. Electronic, dielectric, and optical properties of individual composite silver halide microcrystals using the EELS and LMTO-ASA techniques. *Phys. Rev. B* **67**, 115409 (2003).
29. Stoughton, S. et al. Adsorption-controlled growth of BiVO_4 by molecular-beam epitaxy. *Appl. Phys. Lett. Mater.* **1**, 42112 (2013).
30. Shi, Y. et al. Crystal growth and structure and magnetic properties of the 5d oxide $\text{Ca}_3\text{LiOsO}_6$: extended superexchange magnetic interaction in oxide. *J. Am. Chem. Soc.* **132**, 8474–8483 (2010).
31. Kanungo, S., Yan, B., Felser, C. & Jansen, M. Active role of nonmagnetic cations in magnetic interactions for double-perovskite Sr_2BOsO_6 (B = Y, In, Sc). *Phys. Rev. B* **93**, 161116 (2016).
32. Perdew, J. P., Burke, K. & Ernzerhof, M. Generalized gradient approximation made simple. *Phys. Rev. Lett.* **77**, 3865 (1996).
33. Feng, H. L. et al. Canted ferrimagnetism and giant coercivity in the nonstoichiometric double perovskite $\text{La}_2\text{Ni}_{1.19}\text{Os}_{0.81}\text{O}_6$. *Phys. Rev. B* **97**, 184407 (2018).
34. Tran, F. & Blaha, P. Accurate band gaps of semiconductors and insulators with a semilocal exchange-correlation potential. *Phys. Rev. Lett.* **102**, 226401 (2009).
35. Taylor, A. E. et al. Magnetic order and electronic structure of the 5d³ double perovskite $\text{Sr}_2\text{ScOsO}_6$. *Phys. Rev. B* **91**, 100406 (2015).
36. Margulies, D. T. et al. Origin of the anomalous magnetic behavior in single crystal Fe_3O_4 films. *Phys. Rev. Lett.* **79**, 5162 (1997).
37. Wakabayashi, Y. K. et al. Electronic structure and magnetic properties of magnetically dead layers in epitaxial $\text{CoFe}_2\text{O}_4/\text{Al}_2\text{O}_3/\text{Si}(111)$ films studied by X-ray magnetic circular dichroism. *Phys. Rev. B* **96**, 104410 (2017).
38. Wakabayashi, Y. K. et al. Cation distribution and magnetic properties in ultrathin $(\text{Ni}_{1-x}\text{Co}_x)\text{Fe}_2\text{O}_4$ ($x = 0-1$) layers on $\text{Si}(111)$ studied by soft x-ray magnetic circular dichroism. *Phys. Rev. Mater.* **2**, 104416 (2018).
39. Koster, G. et al. Structure, physical properties, and applications of SrRuO_3 thin films. *Rev. Mod. Phys.* **84**, 253 (2012).
40. Cai, B. et al. A class of Pb-free double perovskite halide semiconductors with intrinsic ferromagnetism, large spin splitting and high Curie temperature. *Mater. Horiz.* **5**, 961 (2018).
41. Mannhart, J. & Schlom, D. G. Oxide interfaces—an opportunity for electronics. *Science* **327**, 1607 (2010).
42. Hwang, H. Y. et al. Emergent phenomena at oxide interfaces. *Nat. Mater.* **11**, 103 (2012).
43. Naito, M. & Sato, H. Stoichiometry control of atomic beam fluxes by precipitated impurity phase detection in growth of $(\text{Pr,Ce})_2\text{CuO}_4$ and $(\text{La,Sr})_2\text{CuO}_4$ films. *Appl. Phys. Lett.* **67**, 2557 (1995).
44. Yamamoto, H., Krockenberger, Y. & Naito, M. Multi-source MBE with high-precision rate control system as a synthesis method sui generis for multi-cation metal oxides. *J. Cryst. Growth* **378**, 184 (2013).
45. Graebner, J. E., Greiner, E. S. & Ryden, W. D. Magnetothermal oscillations in RuO_2 , OsO_2 , and IrO_2 . *Phys. Rev. B* **13**, 2426 (1976).
46. Greedan, J. E., Willson, D. B. & Haas, T. E. The metallic nature of osmium dioxide. *Inorg. Chem.* **7**, 2461 (1968).
47. Yen, P. C., Chen, R. S., Chen, C. C., Huang, Y. S. & Tjong, K. K. Growth and characterization of OsO_2 single crystals. *J. Cryst. Growth* **262**, 271 (2004).
48. White, D. L., Andrews, S. B., Faller, J. W. & Barnett, R. J. The chemical nature of osmium tetroxide fixation and staining of membranes by X-ray photoelectron spectroscopy. *Biochim. Biophys. Acta* **436**, 577–592 (1976).
49. Hayakawa, Y. et al. X-ray photoelectron spectroscopy of highly conducting and amorphous osmium dioxide thin films. *Thin. Solid. Films.* **347**, 56–59 (1999).
50. Kouvel, J. S. & Fisher, M. E. Detailed magnetic behavior of nickel near its Curie temperature. *Phys. Rev.* **136**, 1626 (1964).
51. Kresse, G. & Hafner, J. *Ab initio* molecular dynamics for liquid metals. *Phys. Rev. B* **47**, 558 (1993).
52. Kresse, G. & Furthmüller, J. Efficient iterative schemes for *ab initio* total-energy calculations using a plane-wave basis set. *Phys. Rev. B* **54**, 11169 (1996).
53. Blochl, P. E. Projector augmented-wave method. *Phys. Rev. B* **50**, 17953 (1994).
54. Kresse, G. & Joubert, D. From ultrasoft pseudopotentials to the projector augmented-wave method. *Phys. Rev. B* **59**, 1758 (1999).
55. Perdew, J. P. Accurate density functional for the energy: real-space cutoff of the gradient expansion for the exchange hole. *Phys. Rev. Lett.* **55**, 1665 (1985).
56. Dudarev, S. L., Savrasov, S. Y., Humphreys, C. J. & Sutton, A. P. Electron-energy-loss spectra and the structural stability of nickel oxide: An LSDA + U study. *Phys. Rev. B* **57**, 1505 (1998).

Acknowledgements

We thank Ken-ichi Sasaki for a valuable discussion, Ai Ikeda for her help with the X-ray diffraction and resistivity measurements, Hiroshi Irie for his help with the resistivity measurements, and Kazuhide Kumakura for his help with the MPMS3 SQUID-VSM oven option.

Author contributions

Y.K. and Y.K.W. prepared the samples. Y.K.W. performed experimental measurements and data analysis. N.T. and S.T. carried out the electronic-structure calculations. Y.K.W. wrote the paper. Y.K.W., Y.K., N.T., T.B., S.T., Y.T., and H.Y. contributed to the manuscript and the interpretation of the data.

Additional information

Supplementary Information accompanies this paper at <https://doi.org/10.1038/s41467-019-08440-6>.

Competing interests: The authors declare no competing interests.

Reprints and permission information is available online at <http://npg.nature.com/reprintsandpermissions/>

Journal peer review information: *Nature Communications* thanks the anonymous reviewers for their contribution to the peer review of this work. Peer review reports are available.

Publisher's note: Springer Nature remains neutral with regard to jurisdictional claims in published maps and institutional affiliations.



Open Access This article is licensed under a Creative Commons Attribution 4.0 International License, which permits use, sharing, adaptation, distribution and reproduction in any medium or format, as long as you give appropriate credit to the original author(s) and the source, provide a link to the Creative Commons license, and indicate if changes were made. The images or other third party material in this article are included in the article's Creative Commons license, unless indicated otherwise in a credit line to the material. If material is not included in the article's Creative Commons license and your intended use is not permitted by statutory regulation or exceeds the permitted use, you will need to obtain permission directly from the copyright holder. To view a copy of this license, visit <http://creativecommons.org/licenses/by/4.0/>.

© The Author(s) 2019